Relevant Turbulent Time Scale for Broadband Sound and the Prediction of the Grid Cut-Off Frequency for LES Based Aeroacoustic Simulations

Eman Bagheri, Florian Wachter[✉], and Stefan Becker

Institute of Fluid Mechanics LSTM, Friedrich-Alexander Universität
Erlangen-Nürnberg, 91058 Erlangen, Germany
{eman.m.bagheri,flo.wachter,stefan.becker}@fau.de
https://www.lstm.tf.fau.de/

Abstract. In this work, we establish a relation between the generation of broadband sound for the inertial subrange in turbulent flows and the turbulence cascade mechanism. A dimensional analysis of the perturbed convective wave equation (PCWE) source term is used to obtain the time scale of the aeroacoustic source term and its relation to the turbulent length scales. Based on these findings, a new method to estimate the grid cut-off frequency (f_{GCO}) is proposed. The frequency f_{GCO} determines the maximum frequency up to which the turbulent structures are fully resolved by the grid of the flow simulation. For hybrid aeroacoustic simulations, this maximum resolvable frequency of the flow simulation also determines the maximum frequency content of the aeroacoustic sources and therefore the highest frequency that can be resolved in the subsequent acoustic simulation of broadband sound. The ability of the new method to estimate the f_{GCO} is tested against two common methods frequently used in literature. The test case of a forward-facing step is chosen which is a common aeroacoustic benchmark case and known to generate broadband sound. The new method shows promising results when the estimated grid cut-off frequency is compared against the estimations from the two reference methods.

Keywords: broadband sound · turbulent time scale · grid cut-off frequency

1 Relevant Turbulent Time Scale for Broadband Sound

1.1 Energy Cascade and Kolmogorov's Hypothesis

The idea of the energy cascade of turbulence was introduced by Richardson in 1922 and describes the transfer of energy from large scales of turbulent motion to smaller scales. The first basic concept is that turbulence can be considered to be composed of eddies of different sizes. The term eddy is not clearly defined

but is commonly seen as a turbulent motion, localized in a region of size l which is at least moderately coherent over this region [1]. The second basic concept of the energy cascade is that large eddies are unstable, break up and transfer their energy to smaller eddies. This break-up process and energy transfer repeat for every level of smaller eddies until the eddy size and local Reynolds number become so small that molecular viscosity is effective in dissipating the kinetic energy of the smallest eddies.

For sufficiently high Reynolds numbers and within the universal equilibrium range, the transfer of energy to successively smaller scales is equal to the turbulent dissipation rate ϵ [1]. When the size of the eddy l is within the inertial subrange, an associated timescale τ_l can be defined. The time scale τ_l is referred to as the eddy turnover time, and it describes the time it takes for an eddy of length-scale l to break up into eddies of the next smaller level (say lengthscale $l/2$). From this definition and using dimensional analysis, an associated velocity scale u_l can be introduced

$$u_l \sim \frac{l}{\tau_l} \tag{1}$$

The dissipation rate of the turbulent kinetic energy ϵ can be obtained and related to u_l and τ_l by

$$\epsilon \sim \frac{u_l^2}{\tau_l} \sim \frac{u_l^3}{l} \ , \tag{2}$$

and by combining Eq. 1 and 2 a relation between the time and length scales can be acquired

$$\tau_l \sim \epsilon^{-\frac{1}{3}} l^{\frac{2}{3}} \ . \tag{3}$$

The pressure fluctuations associated with a turbulent motion of size l can therefore be defined as

$$p_l \sim \rho u_l^2 \sim \rho \epsilon^{\frac{2}{3}} l^{\frac{2}{3}} \ . \tag{4}$$

Thereafter, the derivative of pressure p_l for an eddy in the Lagrangian frame can be approximated. Considering the break-up of an eddy with lengthscale l into smaller eddies of lengthscale $l/2$ over the period τ_l, it yields

$$\frac{dp_l}{dt} \sim \frac{\rho \epsilon^{\frac{2}{3}} l^{\frac{2}{3}} - \rho \epsilon^{\frac{2}{3}} \left(\frac{l}{2}\right)^{\frac{2}{3}}}{t + \tau_l - t} \sim \frac{\rho \epsilon^{\frac{2}{3}} l^{\frac{2}{3}}}{\tau_l} \ . \tag{5}$$

The turbulent kinetic energy is distributed among the eddies of different sizes. The turbulent motions of lengthscale l correspond to the wavenumber $\kappa = 2\pi/l$. The total turbulent kinetic energy k is obtained by integrating the energy spectrum over the whole wavenumber space

$$k = \int_0^\infty E(\kappa) d\kappa \ . \tag{6}$$

From Kolmogorov's second similarity hypothesis it follows that the energy spectrum function $E(\kappa)$ can be described in the inertial subrange as

$$E(\kappa) = C \epsilon^{2/3} \kappa^{-5/3} \ , \tag{7}$$

where C is a universal constant with $C \approx 1.5$.

1.2   Dimensional Analysis of the PCWE Acoustic Source Term

In this section, a dimensional analysis of the source term of the *perturbed convective wave equation* (PCWE) is carried out to relate the turbulent energy cascade to the primary mechanisms of broadband sound generation for the inertial subrange. The PCWE fully describes acoustic sources generated by incompressible flow structures and their wave propagation through flowing media. By introducing the acoustic scalar potential Φ_a, the speed of sound c_0, and the density ρ_0 of the acoustic medium, the perturbed convective wave equation is defined by

$$\frac{1}{c_0^2}\frac{D^2\Phi_a}{Dt^2} - \frac{\partial^2\Phi_a}{\partial x_i^2} = -\frac{1}{\rho_0 c_0^2}\frac{D\hat{p}}{Dt} \ , \quad \frac{D}{Dt} = \frac{\partial}{\partial t} + \overline{U_i}\frac{\partial}{\partial x_i} \ . \tag{8}$$

Considering that the turbulent velocity fluctuations u_i are much smaller than the mean flow velocity $\overline{U_i}$, the derivative of the incompressible pressure fluctuation $D\hat{p}/Dt$ can be approximated as the time derivative of the pressure fluctuation $d\hat{p}/dt$ in the Lagrangian frame, so that the PCWE source term S_{pcwe} can be approximated as

$$S_{pcwe} = -\frac{1}{\rho_0 c_0^2}\frac{D\hat{p}}{Dt} \approx -\frac{1}{\rho_0 c_0^2}\frac{d\hat{p}}{dt} \ . \tag{9}$$

A similar relation was derived by [2] for the noise source term of fine-scale turbulent structures using the gas kinetic theory analogy and considering fine-scale turbulence as small blobs of fluid moving randomly. Using Eq. 3 and Eq. 5, the dimensional analysis of the acoustic source term S_{pcwe} associated with the turbulent motion of lengthscale l results in

$$S_{pcwe}^l \sim \frac{1}{\rho_0 c_0^2}\frac{dp_l}{dt} \sim \frac{\rho}{\rho_0 c_0^2}\frac{\epsilon^{\frac{2}{3}}l^{\frac{2}{3}}}{\tau_l} \sim \frac{\rho}{\rho_0 c_0^2}\frac{l^2}{\tau_l^3} \sim \frac{\rho\epsilon}{\rho_0 c_0^2} \tag{10}$$

and reveals the dependency of the acoustic source term on the dissipation rate ϵ and the eddy-turnover time τ_l. This dependency, which was established from the perspective of dimensional analysis, implies that the primary mechanism of broadband sound generation in the inertial subrange is related to the turbulence cascade mechanisms.

2   Estimation of the Grid Cut-Off Frequency for LES-Based Aeroacoustic Simulations Regarding Broadband Sound

2.1   Problem Description

The *hybrid* aeroacoustic approach utilizes a separate treatment of the flow and the acoustic fields. In the first step, a scale-resolving flow simulation computes the near-field flow quantities from which acoustic source terms are obtained. Subsequently, the acoustic source term is used to compute the acoustic wave propagation in a separate simulation.
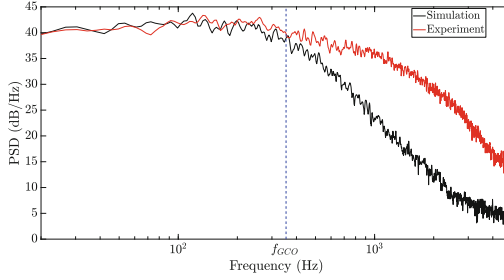
Fig. 1. Comparison of broadband sound spectra from simulation data and experiment. (Color figure online)

Large-eddy Simulation (LES) is widely used to compute the transient, turbulent flow fields. However, LES only resolves the turbulent eddies up to a certain lengthscale, often implicitly determined by the numerical grid of the flow simulation. The effect of turbulence that is not resolved by the grid is usually incorporated by a subgrid-scale model. Therefore, the maximum resolved wavenumber of the turbulent structures is set by the grid resolution. Besides the time-step increment in combination with the *Nyquist* theorem, the maximum resolved wavenumber in the flow simulation determines the maximum frequency content of the acoustic source terms, hence the maximum resolvable frequency in a subsequent acoustic simulation. Figure 1 exemplifies the broadband sound spectrum obtained from a hybrid aeroacoustic simulation in comparison to measurement data. Despite a sufficiently fine time-step and a well-refined acoustic grid, there exists a cut-off frequency beyond which the sound spectrum from the simulation trails off from the measurement data. This cut-off frequency is attributed to the resolution of the flow simulation grid. Therefore, such a behaviour indicates a lack of spatial resolution in the flow computation which leads to an underprediction of the sound pressure level [3]. Since in most acoustic applications, the maximum frequency of interest is known prior to the simulation; it is necessary to choose the grid resolution of the flow simulation such that the grid cut-off frequency (e.g. f_{GCO} in Fig. 1) matches the highest frequency of interest.

2.2   Two Frequently Used Approaches in Literature

There are two common methods available in the literature to determine the grid cut-off frequency f_{GCO} which is used to ensure that the acoustic source region is resolved up to the frequency of interest. Ideally, such methods should predict the f_{GCO} based on RANS (Reynolds-Averaged-Navier-Stokes) simulation data prior to the expensive LES and acoustic simulations. For both methods, the grid cut-off wavenumber $\kappa_{GCO} = 2\pi/2\Delta = \pi/\Delta$ is obtained from the *Nyquist* theorem in which Δ is the grid cell length. According to the *Nyquist* theorem, at least two grid cells per lengthscale are required to resolve a given wavenumber [4]. The first method (M1) is based on Taylor's frozen turbulence hypothesis. Thus,

it relates the maximum resolved wavenumber and frequency to the convection velocity U_c and estimates the f_{GCO} via Eq. 11.

$$f_{GCO} = \frac{U_c \, \kappa_{GCO}}{2\pi} = \frac{U_c}{2\Delta} \tag{11}$$

The convection velocity U_c is defined as the velocity by which the turbulent eddy structures are transported downstream. Considering the mechanism of broadband sound generation explained in the previous section using Eq. 10, the frozen turbulence hypothesis is unsuitable for estimating the timescale in the inertial subrange. Furthermore, Eq. 11 assumes a wave-like propagation with a constant velocity for turbulent fluctuations, thus establishes a linear relationship between frequency and wavenumber. This is incompatible with the physics of turbulence and contrary to findings of the dimensional analysis presented in the previous section in Eq. 3. As a result, method M1 typically overestimates the cut-off frequency.

The second method (M2) was introduced by Mendonça [5] (see also [3]). This method attempts to address the problem of the frozen turbulence hypothesis in M1 by incorporating the turbulent kinetic energy into the equation. The grid cut-off frequency based on M2 is given in Eq. 12.

$$f_{GCO} = \frac{\sqrt{\frac{2}{3}k}}{2\Delta} \tag{12}$$

Although turbulence is taken into account by method M2, it still suffers from the assumption that the wavenumber and frequency are linearly related. This is simply because a wave-like propagation is assumed as in M1, but the propagation speed is changed to be the root mean square of the velocity fluctuations. Furthermore, the spectral distribution of the turbulent kinetic energy across different lengthscales is ignored. As velocity fluctuations are orders of magnitude smaller than the convection velocity, this method predicts much smaller cut-off frequencies compared to M1, often underestimating the f_{GCO} as it is shown in the upcoming Sect. 2.4.

2.3   A New Method to Estimate the Grid Cut-Off Frequency

In this section, we propose a new grid cut-off estimation method (M3) using the findings from dimensional analysis and considering the spectral distribution of turbulent quantities. The dependency of the acoustic source term on the dissipation rate and the eddy-turnover time in Eq. 10 implies that the primary mechanism of broadband sound generation in the inertial subrange is the turbulence cascade. Therefore, the frozen-turbulence hypothesis used in method M1 is invalid for the aeroacoustic sound generation of the inertial scales. The relation from Eq. 10 also explains why acoustic sources are dominant on solid walls where the turbulence dissipation rate is at its maximum. Therefore, the local turbulence intensity should not be considered as an indicator of the acoustic source intensity. Instead, the dimensional analysis shows that the source intensity for

the inertial scales is attributed to the local turbulence dissipation rate. This is partly the reason why Eq. 12 leads to large errors in proximity to the wall where production and dissipation are not locally in balance. Moreover, Eq. 10 reveals that the eddy turnover time is indeed the relevant timescale for the acoustic source term generated by the inertial scales. The relation between the time and length scales in Eq. 3 shows that the assumption of a linear relationship between time and length scales (frequency and wavenumber) in M1 and M2 is inaccurate. As l is located in the inertial subrange, Eq. 3 can be rewritten as a function of wavenumber $\kappa = 2\pi/l$ using Kolmogorov's model for the energy spectrum of a fully turbulent flow (Eq. 7) to obtain the eddy turnover time τ_κ as a function of wavenumber:

$$\tau_\kappa = [\kappa^3 E(\kappa)]^{-\frac{1}{2}} = C^{-\frac{1}{2}} \epsilon^{-\frac{1}{3}} \kappa^{-\frac{2}{3}} \ . \tag{13}$$

The maximum wavenumber resolved by the grid in an LES with implicit filtering is $\kappa_{GCO} = 2\pi/2\Delta$, in which Δ is the local grid spacing. Thus, the grid cut-off frequency $f_{GCO} = \tau_{GCO}{}^{-1}$ follows from Eq. 13:

$$f_{GCO} = C^{\frac{1}{2}}[\epsilon \ \kappa_{GCO}^2]^{\frac{1}{3}} = C^{\frac{1}{2}}[\epsilon \ (\pi/\Delta)^2]^{\frac{1}{3}} \ . \tag{14}$$

Our proposed cut-off estimation method M3 in Eq. 14 expresses the dependency of the cut-off frequency on the turbulence dissipation rate. This is consistent with our analysis in Eq. 10 in which ϵ proves to play the key role in broadband sound generation by the inertial eddies. Furthermore, the spectral distribution of the turbulent kinetic energy and timescale of the turbulence cascade is built into M3. Consequently, this criterion provides an accurate estimation for the grid cut-off frequency, as will be discussed in the next sections.

2.4   Approach to Compare the Methods

To verify the capability of the proposed method for an accurate estimation of f_{GCO}, we performed wall-resolved large-eddy simulations on three numerical grids with different resolutions. The open-source code OpenFOAM was used for the simulations. A forward-facing step (FFS) was chosen as the testcase, which is a common aeroacoustic benchmark case and is known to generate broadband sound. As the present work considers transient, low Mach number flows (Ma^2 $\ll$ 1), we chose a finite volume-based LES with an incompressible, isothermal formulation. To model unresolved scales, the WALE (Wall-Adapting Local Eddy-Viscosity) subgrid-scale model was used. Additionally, RANS simulations were carried out with the k-ω-SST turbulence model with no wall-functions applied.

In Fig. 2, a lateral view of the simulation domain is shown. The step has a height h of 12 mm and faces an incoming turbulent boundary layer with a thickness $\delta \approx 11$ mm. The Reynolds number based on h is about 8000. A no-slip boundary condition is applied on the boundaries indicated with w in Fig. 2. Slip conditions are used at the boundaries labeled with s and periodic conditions are utilized at the lateral boundaries (perpendicular to the image plane). At the outlet o, a Neumann condition is applied. The method to develop a boundary layer with thickness δ was adopted from [6]. A recycling plane was used (indicated

in red in the left part of Fig. 2) to map the velocity field back to the inlet boundary m. At the other inlet boundary u, a constant freestream velocity is set. 200 probes are distributed in the flow field domain for further spectral analyses. For the sake of brevity, we focus on the results extracted from probes P1 and P2 shown in Fig. 2 as they represent the spectral behaviour observed in other probes. Probe P1 is positioned in the region where an attached fully developed turbulent boundary layer is present and P2 is located in the wake region of the step.
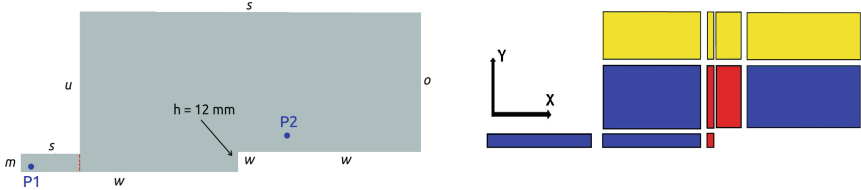
Fig. 2. Left: Simulation domain in side view with probe positions (P1, P2) and boundary conditions, e.g. (m) inlet velocity mapped from the recycling plane shown with a red dotted line, (u) fixed freestream inlet velocity, (o) outlet with Neumann condition, (s) walls with slip and (w) no-slip condition. Right: Block divisions used for the block-structured grid. The colours of the blocks indicate different refinement strategies. (Color figure online)

A fully orthogonal, block-structured grid was used for the simulations. The different block types are sketched in Fig. 2 (right). The yellow blocks indicate the turbulent-free regions where a relatively coarse grid resolution is required. The grid is uniform in the streamwise direction except in red blocks where a streamwise refinement was applied near the step. The *coarse* grid has a dimensionless cell width of $\Delta x^+ = 150$ in streamwise, $\Delta y^+ = 0.8 - 8$ in wall-normal, and $\Delta z^+ = 20$ in spanwise directions. The *medium* grid has a dimensionless cell width of $\Delta x^+ = 80$ and for the *fine* grid $\Delta x^+ = 30$. The spanwise and wall-normal resolutions are identical for all three grids. Note that for the comparison of the methods, the LES filter width Δ is set to be the maximum edge length of each cell. This means that the filter width is equal to the streamwise cell width except for a few cells near the step.

The local mean velocity $\overline{U}$ and the turbulent kinetic energy k computed from the LES of the *fine* grid are used as the input data for methods M1 and M2 respectively. The turbulence dissipation rate ϵ needed for method M3 is also obtained from the *fine* grid LES and is later compared to the result from the k-ω-SST RANS simulation. The dissipation rate was determined from the RANS simulation by the relation $\epsilon = \beta^* \omega k$, with $\beta^* = 0.09$ [7].

2.5   Results

Figure 3 (left) shows the resulting energy spectra at point probe P1 from LES with three different grids. The spectrum obtained from the *coarse* grid clearly

trails off from that of the *medium* and *fine* grids. For the *coarse* grid, method
M3 ("cutoff_Spectral") estimates the grid cut-off frequency to be at 362 Hz quite
accurately. Method M1 ("cutoff_Taylor") results in an overestimated cut-off fre-
quency 973 Hz, conversely, method M2 ("cutoff_Mendonça") underestimates it
to be 74 Hz. A similar tendency can be found when the spectra from the *medium*
and *fine* grids are compared. Again, the predicted $f_{GCO} = 539$ Hz from method
M3 fits best to the frequency where the spectrum of the *medium* grid starts to
dwindle away. Once more, M1 overestimates and M2 underestimates the cut-off
frequency.

In Fig. 3 (right), the M3 criterion using LES and RANS results are compared
for probe P1. The criterion using the turbulence dissipation rate obtained from
k-ω-SST somewhat overestimates the grid cut-off frequency in comparison to
the accurate prediction based on the LES data. This error is mainly due to the
eddy-viscosity hypothesis as well as other simplifications made in the RANS
model.
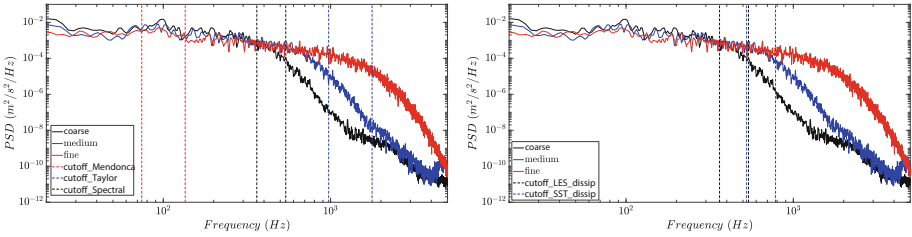
Fig. 3. Energy spectra from LES at probe position P1. Estimated f_{GCO} from the
different methods are indicated based on LES data (left). Estimated f_{GCO} based on
M3 from RANS data in comparison to f_{GCO} from LES data (right). (Color figure
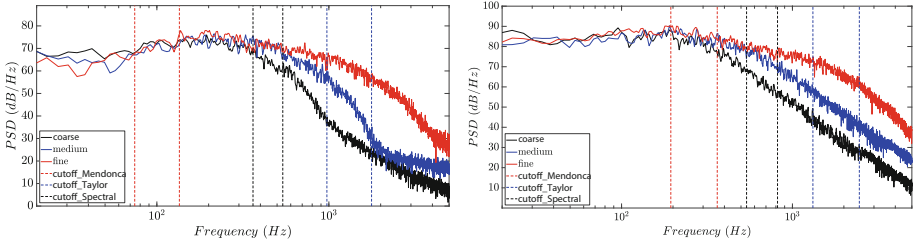online)

Figure 4 (left) presents the energy spectra obtained from probe P2 located
after the step in which a similar trend regarding the performance of the different
methods is observed.
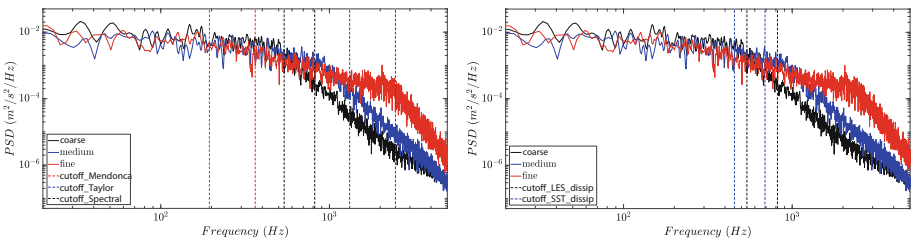
Fig. 4. Energy spectra from LES at probe position P2. Estimated f_{GCO} from the
different methods are indicated based on LES data (left). Estimated f_{GCO} based on
M3 from RANS data in comparison to f_{GCO} from LES data (right). (Color figure
online)

Figure 4 (right) is a similar plot as in Fig. 3 (right) but for the probe P2, where the method M3 based on the RANS data slightly underestimates the cut-off frequency in comparison to the LES based approach. However, even with incorporating less accurate RANS modelled data into the M3 criterion, it still outperforms the other two methods fed with accurate LES-resolved data (compare both plots of Fig. 3 against each other, and both plots in Fig. 4).

Fig. 5. Pressure spectra from LES at probe position P1 (left) and P2 (right). Estimated f_{GCO} from the different methods are indicated based on LES data. (Color figure online)

In Fig. 5, the obtained pressure spectra from position P1 and position P2 are shown together with the f_{GCO} predictions based on LES data. The pressure spectra at P1 (Fig. 5, left) show that the method M3 accurately estimates the f_{GCO}. Obviously, method M1 overestimates and method M2 underestimates the f_{GCO}. The pressure spectra at position P2 (Fig. 5, right) do not show such a clear superiority of method M3 over M2. While the spectra reveal a f_{GCO} of 600 Hz for the medium mesh, method M3 predicts $f_{GCO} \approx 717$ Hz and M2 $f_{GCO} \approx 363$ Hz. For the coarse mesh, the spectra show a f_{GCO} of 300 Hz. Method M3 estimates $f_{GCO} \approx 538$ Hz and M2 predicts $f_{GCO} \approx 194$ Hz. Regarding the pressure spectra at P2, both methods, M2 and M3, predict the f_{GCO} with an offset of about the same magnitude, with M2 underestimating and M3 overestimating the f_{GCO}. It is noteworthy that in comparison to M2, method M3 predicts the f_{GCO} for the medium mesh more accurately where the LES grid resolves finer turbulent structures and the assumption of the LES filter lying in the inertial subrange is more substantiated. Method M1 shows the worst performance in predicting the f_{GCO} in Fig. 5 (right).

2.6 Summary and Final Remarks

Using the dimensional analysis of the PCWE source term, an aeroacoustically relevant timescale for the inertial subrange was obtained and its relation to turbulence lengthscales was derived. Subsequently, the grid cut-off estimation method M3 was proposed. As expected from the dimensional analysis, the new method performs best for the FFS test case and the prediction of f_{GCO} always lies between that of the M1 and M2. However, method M3 requires reasonably

accurate data for the local turbulence dissipation rate to provide valid estimations. As the accuracy of RANS models, especially in regard to ϵ varies from case to case, choosing an appropriate turbulence model is essential for accurate cut-off frequency estimations. As the energy spectra reveal, our proposed method based on RANS data still predicts the f_{GCO} more accurately than the other methods M1 and M2 do with LES data.

As a final remark, the authors want to emphasize that the method to estimate the mesh cut-off frequency is only an additional mesh resolution criterion to ensure that the highest frequency of interest is resolved within the relevant acoustic source region (see Sect. 2.1). All other essential criteria required for a proper large-eddy simulation should be additionally met. To give some examples: the LES filter width should lie within the inertial subrange as suggested, among others, by [1] and [4]. As a rule of thumb, Pope [1] recommends to resolve about 80% of the turbulent kinetic energy. For wall-bounded flows, near-wall mesh resolution requirements are given and discussed in [3].

References

1. Pope, S.: Turbulent Flows. Cambridge University Press, Cambridge (2000)
2. Tam, A.: Jet mixing noise from fine-scale turbulence. In: 4th AIAA/CEAS Aeroacoustics Conference (1998)
3. Wagner, C., Hüttl, T., Sagaut, P.: Large-Eddy Simulation for Acoustics, vol. 20. Cambridge University Press, Cambridge (2007)
4. Davidson, L.: Fluid mechanics, turbulent flow and turbulence modeling. Div. of Fluid Dynamics, Dep. of Applied Mechanics, Chalmers University of Technology, Göoteborg, Sweden (2019)
5. Mendonça, F., Read, A., Caro, S., Debatin, K., Caruelle, B.: Aeroacoustic simulation of double diaphragm orifices in an aircraft climate control system. In: 11th AIAA/CEAS Aeroacoustics Conference (2005)
6. Scheit, C.: Hybrid aeroacoustic methods for broadband noise calculation. PhD thesis, Friedrich- Alexander-Universität Erlangen-Nürnberg (FAU) (2016)
7. Wilcox, D.C.: Turbulence Modeling for CFD, 2nd edn. DCW Industries Inc. (2004). ISBN 1-928729-10-X